Master's program in Advanced energy solutions

Ion beam mixing in tungsten predicted with a novel two-temperature molecular dynamics model

Iisa Saunamäki

Aalto University

MASTER'S
THESIS

Aalto University
MASTER'S THESIS 2022

Ion beam mixing in tungsten predicted with a novel two-temperature molecular dynamics model

Iisa Saunamäki

Thesis submitted in partial fulfillment of the requirements for the degree of Master of Science in Technology.
Otaniemi, 30 May 2022

Supervisor: Professor Andrea Sand
Advisor: Professor Andrea Sand

Aalto University
School of Electrical engineering
Master's Programme in Anvanced energy solutions

Author
Iisa Saunamäki

Title
Ion beam mixing in tungsten predicted with a novel two-temperature molecular dynamics model

School School of Electrical engineering

Master's programme Advanced energy solutions

Major Sustainable energy systems and markets **Code** ELEC3048

Supervisor Professor Andrea Sand

Advisor Professor Andrea Sand

Level Master's thesis **Date** 30 May 2022 **Pages** 52 **Language** English

Abstract

Plasma-facing materials in fusion reactors are exposed to high doses of irradiation, causing radiation damage to the materials. The characterization of the damage is crucial for the research of fusion-relevant materials. However, a major outstanding open question remains about how electronic excitation affects the radiation damage process.

The project involves performing atomistic simulations of radiation-induced collision cascades, using a newly developed model that explicitly accounts for electronic energy losses in the highly non-equilibrium cascade process. The level of atomic mixing, which is experimentally known as ion-beam mixing, is conjectured to be sensitive to the coupling between electronic and atomic systems. In this work, the atomic mixing was analyzed from the simulations and compared to experimentally derived values for tungsten, to gauge the model accuracy.

The values of atomic mixing obtained by using the model are in a good agreement with the experimental values. We employ two different functions for the coupling between the atomic and electronic systems, displaying different strengths of the electron-phonon coupling. Our results show that the strength of the electron-phonon coupling does not significantly affect the predicted level of atomic mixing.

Keywords radiation damage, collision cascade, molecular dynamics simulations, electron-phonon coupling, ion-beam mixing, dissipation model

Tekijä
Iisa Saunamäki

Työn nimi
Atomistinen sekoitus volframissa käyttäen uutta kahden lämpötilan mallia

Korkeakoulu Sähkötekniikan korkeakoulu

Maisteriohjelma Advanced energy solutions

Pääaine Sustainable energy systems and markets **Koodi** ELEC3048

Valvoja Professori Andrea Sand

Ohjaaja Professori Andrea Sand

Työn laji Diplomityö **Päiväys** 30.5.2022 **Sivuja** 52 **Kieli** englanti

Tiivistelmä

Tulevien fuusioreaktoreiden materiaalit altistuvat reaktorissa korkeille säteilyannoksille aiheuttaen materiaaleihin säteilyvaurioita. Näiden karakterisointi on oleellinen osa fuusiorelevanttien materiaalien tutkimusta. Vuosisadan tutkimuksista riippumatta elektronien virittymisen vaikutus säteilyvaurioiden muodostumiseen on edelleen merkittävä ratkaisematon kysymys.

Tässä työssä mallinnetaan säteilyn aiheuttamia törmäyskaskadeja atomististen simulaatioiden avulla. Simulaatioissa käytetään uutta mallia, joka erityisesti ottaa mukaan elektroniset energiahäviöt erittäin epätasapainoisessa kaskadiprosessissa. Atomien sekoittumisen on arveltu olevan herkkä elektronisen ja atomijärjestelmän väliselle kytkennälle. Tämän vuoksi atomien sekoittuvuus on analysoitu simulaatioiden pohjalta ja verrattu vastaaviin kokeellisesti saatuihin arvoille. Työ on tehty volframille, tarkoituksena validoida mallin tarkkuus.

Mallia käyttäen saadut arvot atomien sekoittuvuudesta ovat hyvin lähellä kokeellisia arvoja. Atomien sekoittuvuuksien analysointi eri elektroni-fononi-kytkennöillä osoittaa sen, että kytkennän vahvuus ei vaikuta merkittävästi tuloksiin.

Avainsanat säteilyvaurio, törmäyskaskadi, molekyyli dynamiikan simulaatio, elektroni-fononi-kytkentä, atomistinen sekoittuvuus, kahden lämpötilan molekyyli dynamiikan malli

Contents

1. Introduction

The current situation of increasing energy demand [1] drives the search for additional solutions for producing energy. Additionally, environmental concerns are creating increasing interest in non-fossil fuels. Therefore, different low emission alternatives are constantly being sought in the energy sector. Nuclear fusion is seen as a potential solution for producing low emission energy, since it does not emit carbon dioxide or other harmful greenhouse gases to the atmosphere.

In order to achieve safe, economically viable, and environmentally acceptable energy production from fusion reactors, advanced materials must be found which are able to handle high levels of heat, radiation, and thermo-mechanical stresses, and also be chemically compatible together [2]. Since there are no experimental facilities that can fully replicate the extreme conditions in a future fusion reactor, the computational study for advanced materials is even more important [3]. It is essential to know how materials would act in the future fusion reactor environment, since radiation affects the physical and mechanical properties of materials. This is often harmful to materials, causing hardening, embrittlement, or swelling. Such effects are detrimental to materials in high irradiation environments such as nuclear facilities. Radiation damage in materials can be studied by molecular dynamics simulations, where the physical movements of individual atoms can be analyzed.

The process that causes radiation damage occurs on the order of picoseconds [4], and hence it is challenging to observe directly [5]. Therefore, computational modeling is necessary to understand and predict the effects of radiation on materials. Today's computational modeling techniques that use massively parallel and high-performance computing platforms, and

improved analytical, experimental characterization tools provide the methods to develop experimentally validated models of materials' performance in the fusion energy environment [3].

Simulations of molecular dynamics are ideal for analyzing radiation damage that is produced right after an initial atomic displacement event [6] initiated by a high-energy particle. Current high-performance computing platforms allow the utilization of molecular dynamics simulations with millions of atoms. However, the models used in molecular dynamics simulations rely on various different approximations, hence it is essential to validate predictions by comparison to experimental results. For example, as in molecular dynamics simulations, all atoms are seen as point particles without any internal structure or electrons [6]. Thus energy losses caused by electronic excitation are not accounted for in the simulation. However, in radiation damage simulations, it is important to account for electronic effects since they affect the slowing down process of ions. This can be done via different extensions to the classical molecular dynamics models.

Tungsten is a candidate material for future fusion reactors as both structural and plasma-facing components [7]. It is a promising material for plasma-facing components, since it has a high thermal conductivity, high melting temperature, low sputtering, and low tritium retention [8]. In this thesis, a model that explicitly accounts for electronic energy losses in the collision cascade process, as well as the electron-phonon coupling near equilibrium, is tested via atomic mixing values obtained by molecular dynamics simulations and validated by comparing simulations' results to experimental measurements.

2. Radiation damage in metals

2.1 Radiation damage event

In a radiation damage event, an incident projectile causes displacements in a crystal lattice, due to the transfer of energy from the incident projectile to atoms in the target material. The radiation damage event consists of several distinct processes, which are described as follows:

1. energetic particles interact with the lattice of atoms in the lattice,

2. formation of the primary knock-on atom (PKA), which is the first atom that the incident particle collides with in the material,

3. displacements of atoms,

4. displaced atoms passage through lattice site creating knock-on atoms, and

5. finally the PKA is terminated as an interstitial [9].

As a result of the radiation damage event, there are imperfections in the material structure [9]. Norgett-Robinson-Torrens (NRT) [10] prediction can be used to predict the number of displaced atoms in a given volume of the material [11]. According to the NRT model, the number of displaced

atoms can be calculated as:

$$N_d(T_d) = \begin{bmatrix} 0 & , & T_d < E_d \\ 1 & , & E_d < T_d < 2E_d/0.8 \\ \frac{0.8T_d}{2E_d} & , & 2E_d/0.8 < T_d < \infty \end{bmatrix} \tag{2.1}$$

where E_d is the threshold displacement energy and T_d is energy available for damage production. The threshold displacement energy is the minimum energy that is high enough to displace an atom from its lattice site to the defect position [12]. For a single ion, the energy available for damage production is the nuclear-deposited energy $F_{D,n}$ [4], which represents the amount of energy that is deposited by nuclear collisions to atoms in the material during the slowing down the process. It can be calculated by subtracting the energy lost to electronic stopping from the total particle energy $F_{D,n} = E_0 - F_{D,e}$. The factor 0.8 in NRT equation 2.1 is obtained from binary collision approximation simulations [13].

The NRT equation can be formalized into a unitless quantity, often referred to as displacements per atom (dpa):

$$\text{Dpa} = \frac{\text{Number of displaced atoms in volume from NRT equation}}{\text{Number of material's atoms in the volume}} \tag{2.2}$$

The dpa concept and NRT equation are widely used for quantifying radiation exposure in materials due to their simplicity. Calculations with these equations are very straightforward, and the results can be compared between different materials and irradiating species [4]. However, dpa calculations do not correspond directly to damage production. It is a noted fact that NRT over-predicts the number of defects in metals, where radiation damage does not increase linearly with the energy [13].

2.2 Collision cascades

When a particle that is energetic enough comes in contact with a material, it may undergo elastic collisions with atoms in the material, causing kinetic energy to be transferred to the target atoms [14]. If the atom is energetic enough, it can cause further collisions with the lattice atoms, finally resulting in numerous collisions. This series of consecutive collisions is called a collision cascade [14]. Suppose the energy of an atom after a collision is larger than the threshold displacement energy. In that case, an atom is displaced from its lattice site, leaving either an empty site or an extra atom occupying the site behind [6].

A reasonably dense cascade goes through three main stages during its development. These can be identified based on the momentary number of displaced atoms in the material, as seen in figure 2.1. The first stage is called the ballistic phase, the second the thermal phase, and the third the relaxation phase.

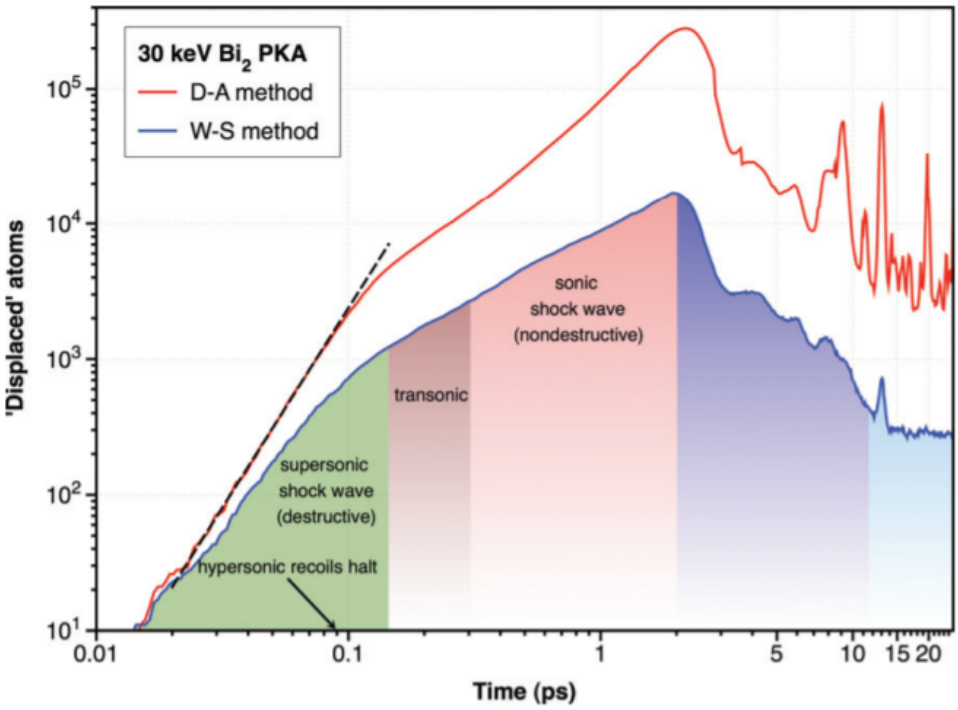

Figure 2.1. The number of displaced atoms during a 30 keV Bi_2 PKA collision cascade evolution in Fe [15].

2.2.1 Ballistic phase

The earliest stage in the collision cascade is called the ballistic phase. During that phase, there are mainly high-energy recoils interacting via binary collisions. The ballistic phase lasts approximately 100-300 femtoseconds which is 10^{-15} of a second. For example, in tungsten, the ballistic phase lasts 200 femtoseconds in 150 keV collision cascade [6].

The behavior during the ballistic phase is destructive, meaning that the region of the cascade is expanding. This is due to the recoils penetrating the undisturbed lattice site. The destructive behavior of the cascade during the ballistic phase is illustrated in figure 2.2, where the area of a collision cascade initiated by a 150 keV recoil increases over time. The color of the atoms indicates the time scale during the ballistic phase. Red indicates 0 femtoseconds, and light blue indicates 200 femtoseconds.

In the ballistic phase, the energy of the recoils is high, and the potential energy in the system grows. Recoils in that phase also have high velocities, and due to that, while interacting with lattice atoms, very little energy is transferred in a more extended range [6].

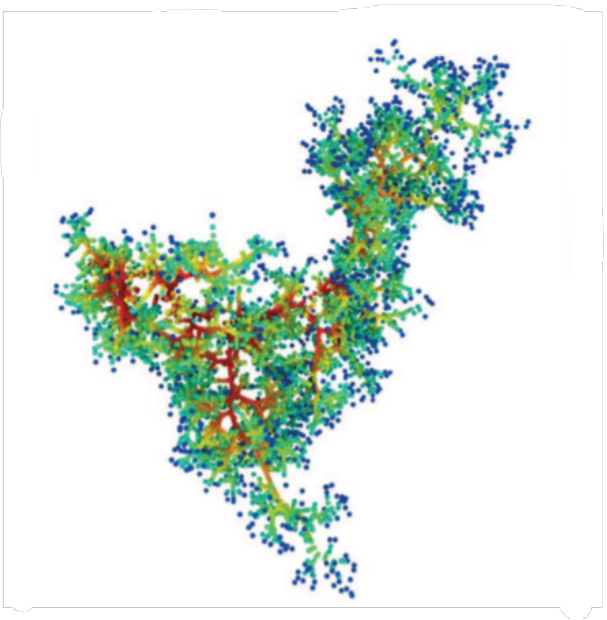

Figure 2.2. Development of a collision cascade over time initiated by 150 keV recoils. The red areas indicate for 0 femtoseconds, and the blue areas indicate for 200 femtoseconds. [16]

2.2.2 Thermal spike and relaxation phase

After the ballistic phase, the collision cascade evolves to a thermal spike. It is a highly disordered area in the core of the cascade. The duration of the thermal spike is on the order of pico-seconds, depending on the PKA energy, the material's melting point, and the ambient temperature [6].

Heat spike is a non-destructive phase of a cascade, and the area no longer expands as in the ballistic phase. However, during this phase, the potential energy in the system keeps growing. Additionally, during a thermal spike, the surrounding materials are being pushed outwards.

During a thermal spike, the number of displaced atoms is strongly overestimated compared the NRT equation (see equation 2.1). However, the final defect count after the cascade cools down is only a fraction of the NRT prediction since the displaced atoms present during the spike recombine when the heat spike cools down.

In the thermal phase, the collective effects such as recombination become important factors to the defect production [17]. The recombination is athermal, meaning that it would also occur when the ambient temperature of the sample is 0 K [13]. Particularly in metals, this athermal recombination is strong [6]. This behavior is illustrated in figure 2.3, where during a heat spike, there are more displaced atoms than in the final composition after the event. After they find their lattice positions for many of the atoms, it is not the initial position they started in. Hence, the amount of relocated atoms is much higher than the amount of produced defects.

The thermal spike dynamics affect the end product of a displacement cascade. It is known to affect atomic mixing, total defect production, and the degree of clustering [18].

After the heat spike, the cascade transitions to the final phase of the collision cascade called the relaxation phase. During that phase, the cascade cools quickly on a time scale of picoseconds, to below the melting point. Interstitials and vacancies may recombine [4], and the highly disordered area of the heat spike shrinks as atoms find lattice positions. The liquid area of the heat spike is recrystallized. Vacancies are pushed towards the

center, and interstitial defects remain on the outskirts [6]. This behavior is illustrated in figure 2.3. The process leaves behind individual point defects and defect clusters as the final product of the displacement cascade [19].

2.3 Ion-beam mixing

Collision cascades are too fast and small to observe directly. Instead the effects after the event can be measured to gauge the correctness of the predictions made in the atomistic simulations. One of these measurements is called atomic mixing, experimentally, ion-beam mixing.

Atomic mixing is the permanent displacement of atoms from their lattice position. The collisions between atoms cause atomic mixing [20]. It can be used to describe the primary state of the radiation damage [13].

As seen from figure 2.4, for heavier metals, the atomic mixing continues for 10 keV cascades up to a few picoseconds. For higher energies, atomic mixing would continue even longer. Hence, for the metals, mixing efficiency is mainly derived from the heat spikes [13]. As ion-beam mixing depends on the duration of the heat spike, the results of ion-beam mixing can be used to determine the correctness of the electronic energy losses in molecular dynamics simulations since the magnitude of electronic losses affects the heat spike directly. Hence, in this thesis, simulated values of atomic mixing are compared to the experimental values of ion-beam mixing.

The experimental procedure for ion-beam mixing is relatively simple since, during irradiation, the atomic mixing occurs at the interface separating the two different materials [20]. The procedure starts first by adding a small layer of impurity of approximately 10 Å in the middle of a material [22]. This layer of impurity is usually called a marker layer. To develop mixing between the marker layer and the material, the marker layer is bombarded with doses of ion radiation. The marker layer is then broadened in a very short time as a result of atomic mixing [23]. From that broadening, the amount of ion-beam mixing can be calculated.

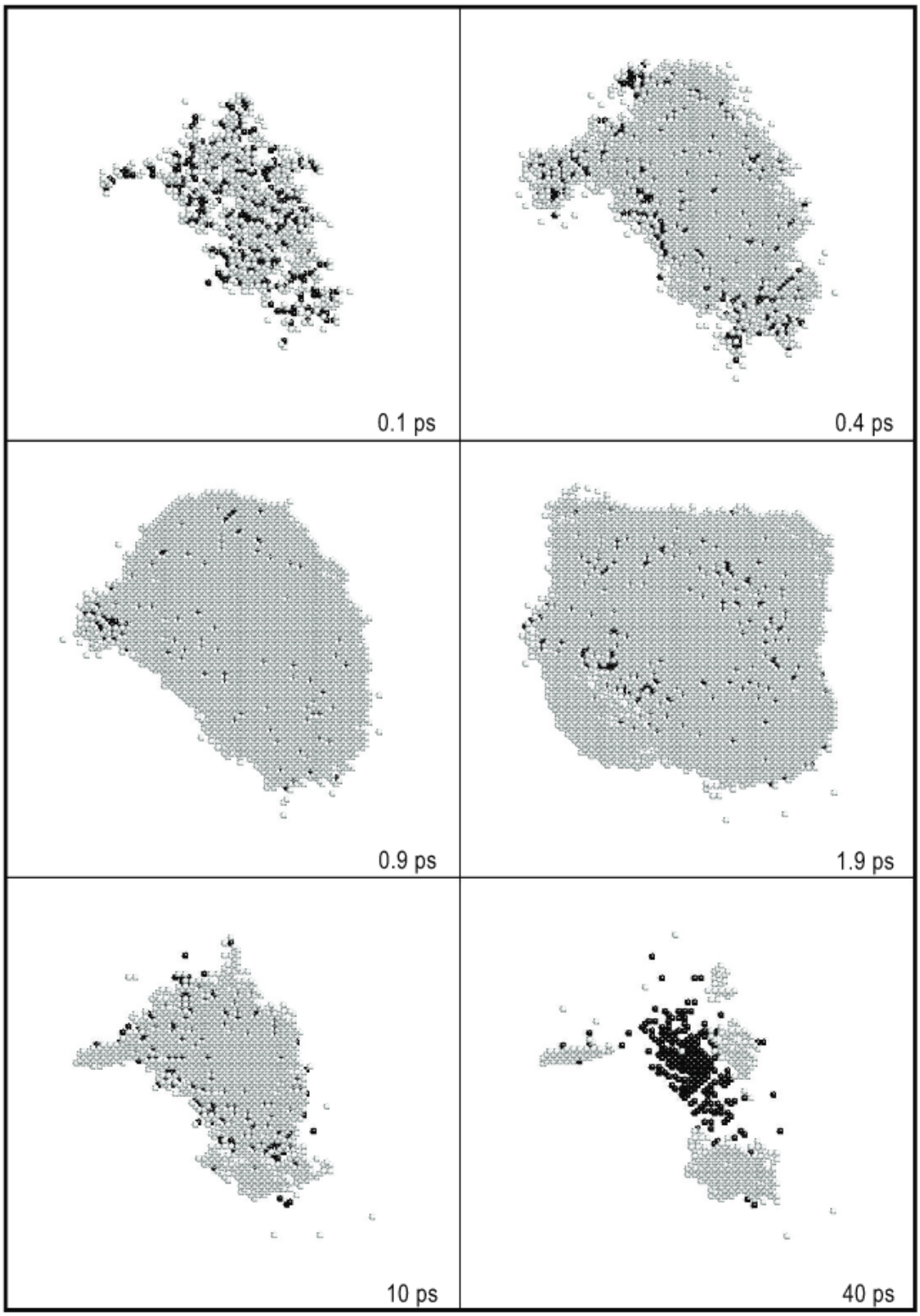

Figure 2.3. Illustration of heat spike evolution until its cooling. Vacancies are black dots and interstitials are white. [6]

Ion-beam mixing is usually obtained from the experiments in terms of the standard deviation σ^2 of the marker layer's broadening. This again can be used to calculate the effective diffusion length $Dt = \sigma^2/2$. [22] Experimentally measured ion-beam mixing can be calculated as follows:

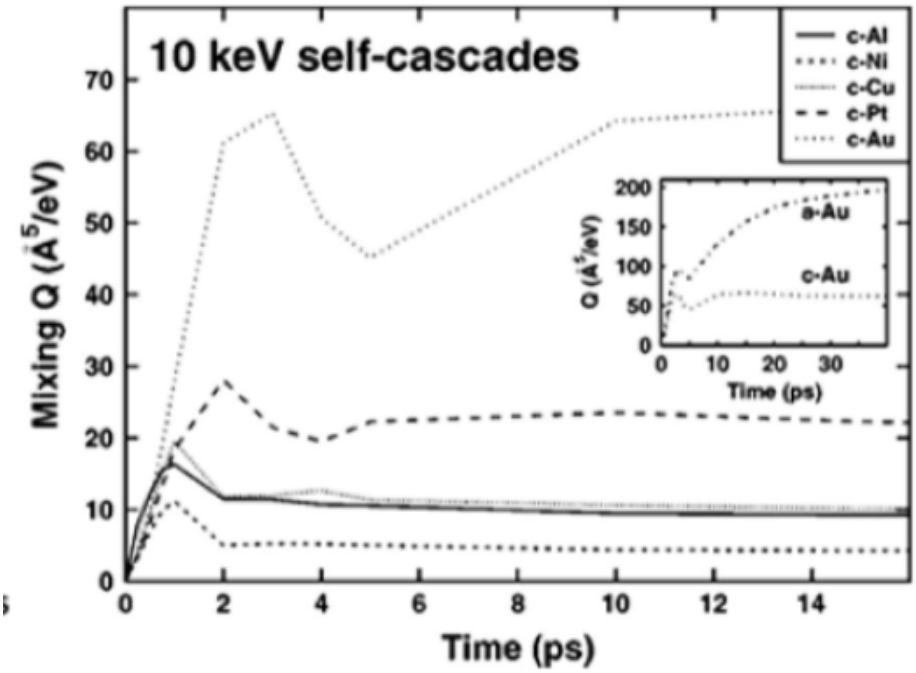

Figure 2.4. Time and atomic mixing evolution of 10 keV cascade for several metals [21].

$$Q_{exp} = \frac{Dt}{\Phi F_{Dn}} \tag{2.3}$$

where D is the effective diffusion coefficient for atomic mixing, t is the implantation time, Φ is the ion fluency, and F_{Dn} is the deposited nuclear energy per ion per unit length [21].

There might be chemical driving forces present in the experimental procedure of ion-beam mixing. For example, the heat of mixing, which is the enthalpy liberated or absorbed from a material upon mixing, might be affecting the results. Negative values of the heat of mixing give a positive driving force to atomic mixing. The presence of chemical driving forces makes it more challenging to compare simulated values to experimental results since these driving forces are not active on the time scale of molecular dynamics simulations.

Large amounts of atoms are displaced in the heat spike, but as it cools down, the displaced atoms recombine. Hence, it is definite that NRT pre-

dictions cannot define atomic mixing [13] and the final count of displaced atoms is only a fraction of the NRT prediction. In order to computationally derive values for atomic mixing, full molecular dynamics simulations are needed. From the simulations, the atomic mixing can be obtained by calculating the averaged atomic relocation caused by primary recoils with different energies. That calculation can be divided into three steps:

1. First, the atomic displacement is obtained by calculating the difference between the final position after picoseconds of simulation time and the initial position after thermalization and then squared.

2. Secondly, the squared displacement values R^2 are all added together as illustrated in the following equation describing the calculation of R^2 values.

$$R^2 = \sum_i (r_i(t) - r_i(t=0))^2 \tag{2.4}$$

3. Thirdly, all the R^2 values obtained from single runs are averaged between the runs of the same energy collision cascade simulations.

In order to interpolate between the averaged R^2 from the cascade simulations, function 2.5 is fitted to the different energy R^2 data points [24]. The averaged R^2 values obtained with different energy are used as data points in the fitting, and a, b, and c fitting parameters.

$$R^2(E) = \frac{aE^{1+c}}{b^c E^c} \tag{2.5}$$

Finally, the atomic mixing efficiency can be determined from $R^2(E)$ 2.5 as follows:

$$Q_{sim} = \int_0^{E_0} \frac{R^2(E)n(E), dE}{6n_0 E_{D_n}} \tag{2.6}$$

where E_0 is the initial energy, n_0 is the atomic density, E_{Dn} is the nuclear deposited energy, and $n(E)dE$ is the recoil spectrum which describes the average number of primary recoils produces in a certain energy interval per implanted ion. Both recoil spectrum and nuclear deposited energy can be obtained from range calculations which are presented in detail in chapter 3.6.

2.4 Defect production in tungsten

Tungsten has a regular crystal structure, similar to other metals. Regular crystal structures can be mathematically described using Bravais lattice [25], which is a way of describing repeating arrangements in space. The lattice is an array of discrete points which are arranged and oriented to look exactly the same at any of the discrete points. The smallest repeating unit is called the unit cell. Tungsten has a lattice structure called body-centered cubic (BCC), which is illustrated in figure 2.5. The atoms are positioned in a BCC unit cell in a cube where there is one atom at each corner and one atom at the center of the unit cell. The corner atoms are shared with eight other unit cells, meaning that in one unit cell corner, there is $\frac{1}{8}$ of the atom.

Defects in the lattice can be considered deviations from a perfect crystalline lattice. Imperfections in the lattice can form, for example, by irradiating the material. As it is known that imperfections in the lattice affect the material's properties [26], it is essential to analyze the radiation-induced defects in the material. Ion-beam mixing can potentially affect the defect

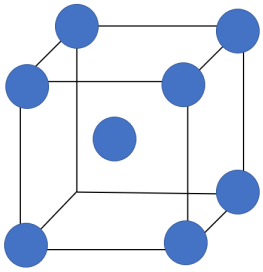

Figure 2.5. BCC structure unit cell.

production in a material. However, it does not necessarily mean that the number of defects increases linearly with atomic mixing. The heat spike phase can last longer, for example, if the electrons heat the cascade. In this case, the mixing could increase, but the number of defects could decrease since they can recombine more easily.

Generally, defects that occur in solids can be divided into four different categories by their dimensions (D):

1. point defects, which are 0-D,

2. dislocations, which are 1-D,

3. external and internal surface, which are 2-D, and

4. volume defects, which are 3-D [26].

Point defect is an imperfection that occurs only at or around a single point of a lattice. These defects are one-dimensional, meaning they do not extend in space in any dimension.

Typical point defects are vacancies and interstitials. A vacancy is a point in the lattice where one atom is missing from its lattice site. Conversely, an interstitial is a point in a lattice where an extra atom is forced to take up a position in the crystal structure that is normally not occupied. [26] a Frenkel pair is a combination of a vacancy and an interstitial. It is primarily formed by particle irradiation, after which some atoms obtain sufficient energy and leave their site leaving behind a vacancy and occupying close

an interstitial position. All these three types of point defects are illustrated in figure 2.6.

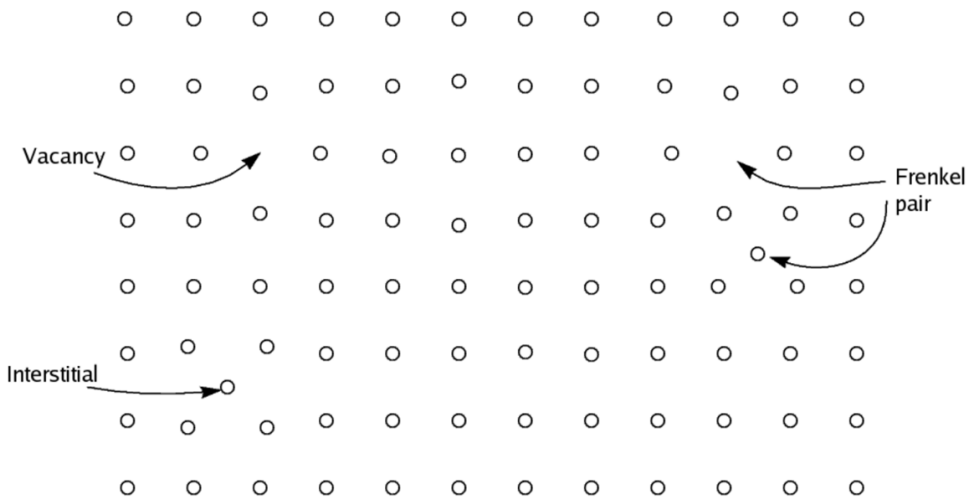

Figure 2.6. Different zero-dimensional defects in monoatomic solid. Modified from [27].

2.5 Stopping effects

Atoms that interact with each other in the medium cause stopping power. For smaller than several hundreds of MeV stopping power can be categorized into two different mechanisms [28] based on where the ion loses its energy:

1. **electronic stopping power** which is is caused by inelastic collisions between the electrons in the material, and

2. **nuclear stopping power** which is due to elastic collision with target atoms' nuclei [29].

Stopping power can be determined by the average energy lost per unit path length as:

$$S = \frac{dE}{dX} \tag{2.7}$$

By combining both, electronic stopping power and nuclear stopping power, the total stopping power can be obtained.

$$S_{tot} = S_e + S_n \tag{2.8}$$

The stopping power can be calculated from the average energy transfer and the mean free path [29] as in equation 2.10. In order to calculate average energy transfer, microscopic cross-sections at projectile energy E and the average energy transfer T are needed [29]. The connection between the average energy transfer and microscopic cross-sections is illustrated in equation 2.9. Dividing that with the mean free path, which is $\lambda = \sigma/N$, the stopping power can be obtained.

$$T = \frac{\int T\sigma dT}{\int \sigma dT} \tag{2.9}$$

$$\frac{dE}{dx} = \frac{T}{\lambda} = \frac{\int T\sigma(E,T)dT}{\int \sigma(E,T)dT} N \int \sigma(E,T)dT = N \int T\sigma(E,T)dT \tag{2.10}$$

As seen from the figure 2.7, electronic stopping dominates the process at the beginning of a slowing down process at higher energies. When the energy of the system decreases, nuclear stopping power becomes more and more likely to happen, and at low enough energies, it dominates the slowing down process [28]. Hence, especially with higher energies, it is

important to take electronic stopping power into account when modeling collision cascades.

Additionally to the electronic stopping power, the electron-phonon cou-

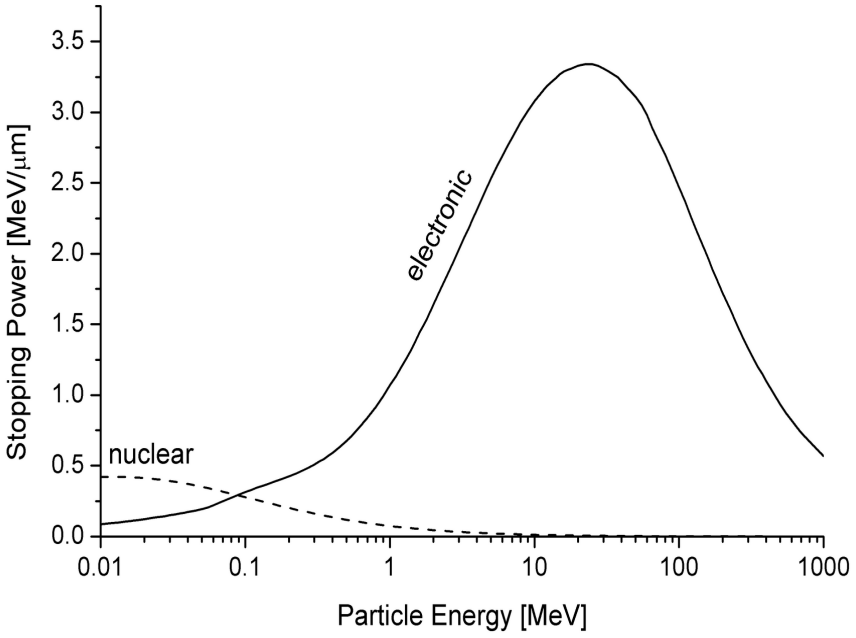

Figure 2.7. Nuclear stopping power and electronic stopping power regimes where electronic stopping power dominates at higher energies [28].

pling has a meaningful effect during the development of a collision cascade. When the electron gas' temperature in a collision cascade rises remarkably, it could lead to an energy feed-back through electron-phonon coupling [30], which is why neglect of electron-phonon coupling might lead to overestimation of the electron's temperature.

3. Molecular dynamics simulations for collision cascades

Molecular dynamics is a computer simulation method used to calculate the motion and the equilibrium of each individual atom or molecule in systems containing up to millions of atoms or molecules. Molecular dynamics (MD) simulations are suitable for describing situations that are not easily observable experimentally. For example, collision cascades can be directly analyzed with MD, whereas experimentally, it is only possible to examine the effects after the event.

3.1 Molecular dynamics algorithm

Classically, molecular dynamics simulations are based on solving the equations of motion for all atoms in the simulated system. In molecular dynamics simulations, atoms are seen as point particles [6], meaning that atoms are simulated without the effect of the internal structure or electrons. Before solving the equations of motion, at the start of the molecular dynamics simulations, all atoms are given initial positions and velocities. MD simulations can be divided into several steps, which are illustrated in a simplified MD algorithm in figure 3.1.

The equations of motion can be expressed by Newton's second law, which describes the forces acting on each atom in the system:

$$m\ddot{r}_i = f_i = \sum_{j=1}^{N_m} f_{ij} \tag{3.1}$$

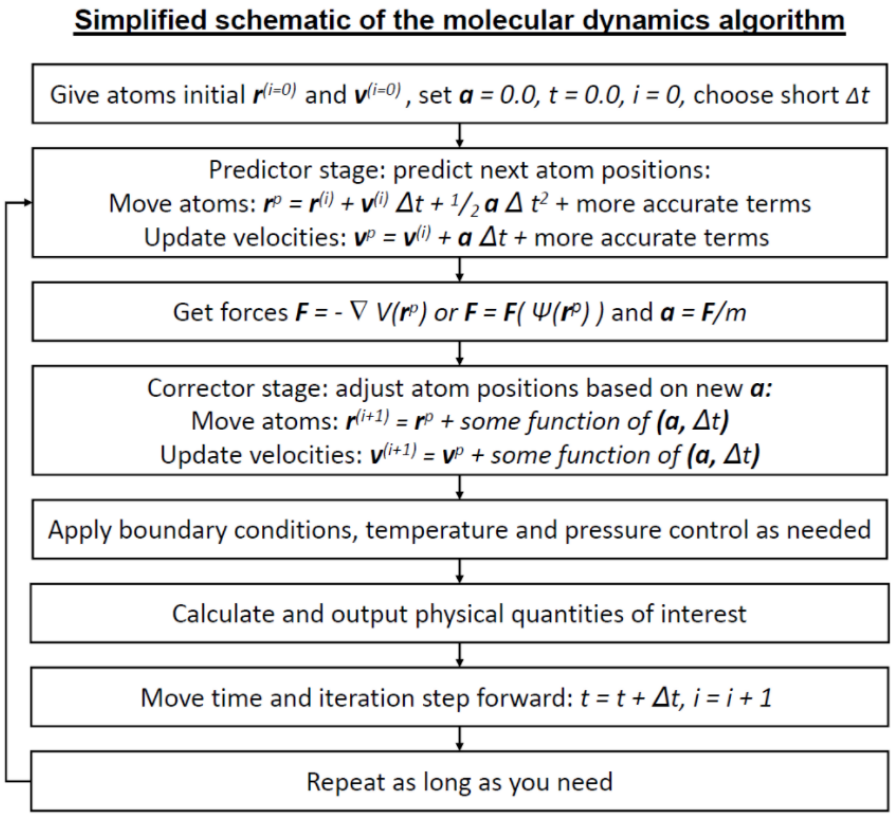

Figure 3.1. Schematic picture of molecular dynamics algorithm, where predictor-corrector integration method is used [31].

$$f_i = -\nabla u(r) \tag{3.2}$$

where r_i, m_i, f_i are position, mass, and force on particle i, and $u(r)$ is the potential energy. Here, the derivative of the interatomic potential gives the force. By numerically integrating over finite time steps, the Newtonian equations can be solved [6].

In practice, there are various procedures to integrate the equations of motion [32]. In this thesis, molecular dynamics simulations were done by using LAMMPS [33] open-source classical molecular dynamics program. It utilizes a leapfrog-type integration method, called the Verlet method for numerically integrating differential equations. It produces coordinates that are accurate to third order in Δt [32]. Furthermore, the storage requirements of the Verlet method are minimal [32].

The Verlet formula is based on the Taylor expansion of the coordinate variable:

$$x(t+h) = x(t) + h\dot{x}(t) + (h^2/2)\ddot{x}(t) + O(h^3) \tag{3.3}$$

where t is the time, $h \equiv (\Delta t)$, $\dot{x}(t)$ is the velocity, and $\ddot{x}(t)$ is the acceleration. By adding a corresponding expansion for $x(t-h)$ to 3.3 and rearranging, equations for calculating positions x at $(t+h)$ are obtained [32]:

$$x(t+h) = 2x(t) - x(t-h) + h^2\ddot{x}(t) + O(h^4) \tag{3.4}$$

The truncation error is of the order of $O(h^4)$ because the h^3 terms cancel [32]. Hence, up to $O(h^4)$ the method is energy conserving [6]. However, computer memory's discreteness introduces numerical errors [6] while utilizing this integration method. This means that in the simulations, the violation of energy conservation is higher than the theoretical level.

3.2 Time step

As mentioned in the previous chapter, when the positions of the atoms are known at one moment, the positions of the next moment's atoms can be found using the integration method.

When the time step is set too large, the atom's motion becomes unstable due to errors that occur during the integration. This could lead to major errors in the conservation of energy. The time step should be small enough so that atoms do not move too far during that step [6]. Conversely, if the time step is set too small, it is also unfavorable since the simulation becomes inefficient. Hence, the selection of the correct time step is crucial.

Usually, one femtosecond is used for the time step in molecular dynamics simulations near equilibrium [34].

A collision cascade is not an equilibrium process. The energy in the system varies over the evolution of the cascade. Initially, the PKA energy is quite high, necessitating a small time step to maintain energy conservation at the early stages of a cascade. However, at later stages, such a small time step is not needed [6]. Using the same time step to simulate during the whole collision cascade evolution is very inefficient, and it uses a lot of resources. This problem can be avoided by using a variable time step, which is an optimization allowing the step size to be as large as possible, while still maintaining an acceptable level of accuracy.

3.3 Interatomic potentials

In molecular dynamics simulations, interatomic potentials describe the interactions between atoms [6]. Hence, the quality of the interatomic potential affects directly to the accuracy of the simulations [35]. A variety of different kinds of information is typical to the calculation of interatomic potentials, including quantum mechanical energy calculations and experimental data, crystalline structures, measurements of transport properties, and molecular collision studies [32]. However, an extensive fitting procedure does not guarantee adequate results in every situation [6].

For many interatomic potentials, there is no need to calculate all interactions between every particle in the simulation with every step since only the interactions between neighboring particles have a significant effect [6]. In many interatomic potentials, a cutoff distance is set to compute only the interactions inside that [32].

Ideally, interatomic potentials should describe all the effects throughout the evolution of a collision cascade in the radiation damage process and beyond. An ideal interatomic potential must consider multiple things, and hence the choice of interatomic potential, in this case, is very crucial. For example, in the ballistic phase of a collision cascade, the interatomic potential must be able to describe interactions at very short distances

[36]. Additionally, since during heat spike there are very high pressures involved, that should be considered while choosing the right interatomic potential. Additionally, a suitable potential should describe interstitial defects, vacancies, and even dislocations produced by the outcome of a cascade [36].

3.3.1 Pair potentials

Pair potentials are the simplest and the earliest interatomic potentials that were developed. In these potentials, the interactions between the atoms are generally described by attractive and repulsive parts. The attractive part is strictly negative, describing the attraction between atoms [37].

The best-known interaction potential is Lennard-Jones (LJ) potential [32], although nowadays there are also better potentials available. The Lennard-Jones extends over a modest range of pair separations. Hence, considerable savings in computing time is obtained by neglecting pair interactions beyond a certain distance [38].

Due to the fact that pair potentials are very simple, they have limitations in atomistic simulations. Pair potentials lack the environmental dependence needed in some situations. In pair potentials, the geometry of surrounding atoms is totally ignored [39], since they cannot be described purely as a function of the interatomic distance between a single pair of atoms. Hence, pair potentials in simulations lead to poorly described surface effects and vacancy formation energy [39]. Additionally, the fact that pair potentials ignore the geometry of the surroundings excludes the possibility of correctly describing BCC elements [39]. One would have to use many-body interatomic potential for BCC elements [39], which accounts for atomic geometry in the atomic system. Hence, pair potentials would not be an option to use in the atomistic simulations of this thesis since we are investigating tungsten which has a BCC structure.

3.3.2 Many-body potentials

In many-body potentials, the atomic geometry is taken into account [37]. It is essential to account since, for metals, the electron clouds responsible for the attractive and repulsive component of the interatomic interactions are not localized close to the individual atoms [32]. Hence, the valence electrons may be shared among atoms, demanding the potential to account for the local electron density, which, consequently, has a many-body nature [32]. These types of potentials are the most used when studying radiation damage in materials [36].

Due to the BCC structure of tungsten, the interatomic potential should account for the second-nearest neighbors. In embedded-atom method (EAM) potentials, interaction with second nearest neighbors can be included, which is one reason an EAM-type potential is used in this thesis in the collision cascade simulations. It is a type of many-body potential based on density-functional theory (DFT), meaning that The fitting targets are generated from DFT calculations for several configurations. EAM-potentials are widely used, especially for metals and alloys [32].

EAM-potentials have two contributions:

1. pair interaction between atoms, which is not density dependent, and

2. a many-body term which depends on the atoms' local value of the electronic density [32].

The two parts of the EAM-potential can be expressed in equation form as:

$$U = \underbrace{\sum_i F_i(\sum_j \rho_j(r_{ij}))}_{1.} + \underbrace{\frac{1}{2}\sum_{ij} \phi_{ij}(r_{ij})}_{2.} \tag{3.5}$$

where F_i is the embedding term, $\rho_{r_{ij}}$ is the local electron density at position i which results from the j positioned atom, ϕ_{ij} is a density-independent

potential, and r_{ij} is the distance between atoms i and j [6]. The local electronic density can be calculated by using DFT. Generally, the term $\rho_j(r_{ij})$ may not be precisely related to the real electron density, but can instead be arbitrarily fitted function [6].

There are different versions of EAM-potentials available. In this thesis a Finnis-Sinclair [40][41] interatomic potential was used. For BCC structured materials, Finnis-Sinclair type potentials are widely used. Here the form of interatomic potential becomes:

$$U = \frac{1}{2}\sum_{i \neq j} \phi(r_{ij}) - A\sum_{i} \sqrt{n_i} \tag{3.6}$$

$$n_i = \sum_{i \neq j} \rho(r_{ij}) \tag{3.7}$$

where the potential parameters are obtained purely by fitting to the available experimental data. The embedding term $F(n_i)$ is $-A\sqrt{n_i}$. The square root is derived from the tight-binding method [42], where the binding energy of the material can be described by two terms: short-range repulsive interactions and attractive interaction. The short-range repulsive interaction can be represented simply by a pair potential that acts between neighboring atoms, and the attractive interaction can be represented by the square root of a sum of pair interactions on the local density [42].

The original EAM potentials do not consider the angular dependence of atoms' positions. In order to include that in the interatomic potential, modified versions of EAM potentials (MEAM) are used. These take into account the directional dependence of electron density. MEAM interatomic potentials are in the same form as EAM potentials, but an angular term is added. In this case, the interatomic potential has the form as follows:

$$U = \sum_{i} F_i(\rho_i) + \frac{1}{2}\sum_{ij} \phi_{ij}(r_{ij}) \tag{3.8}$$

$$\rho_i = \sum_{j \neq i} \rho^a(r_{ij}) + \sum_{k,j \neq i} \rho^a(r_{ij})\rho^a(r_{ik})g(cos\theta_{ijk}) \tag{3.9}$$

where the angle between atoms i, j, and k is described by θ_{ijk}. The atomic electronic density of a type-j atom at distance r_{ij} from site j is described by $\rho^a(r_{ij})$ [43]. However, MEAM potentials have higher computational costs than EAM potentials. Hence, EAM potentials are a better option in this thesis, where multiple similar simulations are done with different energies. Especially at higher energies, where the simulation time is even longer, it is not beneficial to use MEAM potentials.

3.4 Electronic effects in molecular dynamics simulations

In addition to nuclear energy losses, projectiles or recoils experience electronic energy losses. They have a meaningful effect on the MD simulations, so one needs to address them accordingly to obtain accurate results. One can use various methods to implement the effects into molecular dynamics simulations, where electrons are not directly included in the simulations.

3.4.1 Electronic stopping power

In molecular simulations, electronic stopping power can be defined as a frictional force acting on each atom when the kinetic energy is above a certain cut-off. Below the cut-off, the friction is not applied [24]. The choice of the cut-off values is important since it directly affects to the correctness of the energy losses in the simulation [28].

Previously, there has been discussion regarding which cut-off value should be used. For example, Sand. et al. (2015) showed that a 10 eV cut-off value gave more accurate results than a 1 eV cut-off in 200 keV PKA collision cascades in nickel. For a cut-off value of 1 eV, the electronic stopping power

continued into the thermal phase of the cascade, and this underestimated the atomic mixing [24].

The problem with choosing the cut-off accurately can be avoided by using the dissipation model used in this thesis. It bypasses the need of a cut-off value for the electronic stopping power by including the electronic system as a continuum, which is coupled to the ionic system. The thermal state of the electronic system can be solved with a heat equation on a mesh at the same time with the ionic equations of motion [44]. The model is described in more detail in chapter 4.

3.4.2 Electron-phonon coupling

It is also important to account for the electron-phonon coupling in the molecular dynamics simulations. By adding the effects of electron-phonon coupling to the molecular dynamics simulations, one can achieve more accurate results [45] [46].

Electron-phonon coupling controls the return to thermal equilibrium between nuclear and electronic subsystems [47]. It enhances the cooling rate of the heat spike in many metals [48], since thermal conductivity and thermal heat capacity of the electronic systems are otherwise not included in the simulation [49]. The thermal conductivity is handled mainly by the electrons in metals, implying that it is important to account for the electron-phonon coupling in cascades [50].

For tungsten, electron-phonon coupling affects directly the number of defects produced in irradiated metals [51]. The stronger the electron-phonon coupling is, the fewer vacancy dislocation loops are formed in metals.

Electron-phonon coupling can be taken into account in the molecular dynamics simulations by using a two-temperature molecular dynamics model. This is discussed more in detail in chapter 4.

3.5 Boundary conditions and temperature and pressure control

Macroscopic bodies contain far more atoms than one can simulate directly using molecular dynamics [6]. Rather, periodic boundary conditions can be set to simulate larger bulk systems effectively [32]. The simulation box is set to be periodic in the molecular dynamics simulations done for this thesis. This means that the particles in the simulation box can interact across the boundary. In other words, the particles can exit from one end of the simulation box and re-enter again from the other end.

While equilibrating the simulation box, temperature and pressure can be kept constant. This can be done by utilizing thermostats and barostats. In LAMMPS, there are different ways of controlling the temperature, but in this thesis, a Berendsen thermostat is used. In the Berendsen thermostat, the system is coupled to an external bath with a fixed temperature to maintain the temperature [52]. Velocities are scaled at each step so that the rate of temperature change is proportional to the temperature difference:

$$\frac{dT(t)}{dt} = \frac{1}{\tau}(T_0 - T(t)) \tag{3.10}$$

where τ is the coupling parameter determining the tightness between the bath and the system [52]. The scaling factor for velocities is:

$$\lambda^2 = 1 + \frac{\delta t}{\tau}\left(\frac{T_0}{T(t - \frac{\delta t}{2})} - 1\right) \tag{3.11}$$

where $T(t - \frac{\delta t}{2})$ is used because for time integration [52], the leap-frog algorithm is used. This is not a canonical ensemble, but it is applicable for collision cascade simulations [6] of this thesis, which are out of equilibrium. Berendsen thermostat does not perform time integration. It only modifies velocities to affect thermostating.

In the Berendsen barostat, the pressure is regulated by adjusting the

volume of the simulated system. The barostat algorithm changes the volume by an increment proportional to the difference between the internal pressure and pressure in a weakly coupled bath to regulate the pressure [53]. The pressure is given by:

$$P = \frac{1}{V}(\sum_{i} m_i v_i v_i^T + \sum_{i<j} r_{ij} F_{ij}) \tag{3.12}$$

where the first part of the equation is the ideal gas law describing the part where there are no interactions between atoms. The second part is the internal force acting on each atom of the system. The scaling factor of the system is given by:

$$\eta = (1 - \frac{\Delta t}{t_p}(P_0 - P))^{1/3} \tag{3.13}$$

where t_p is the time constant [53].

3.6 Range calculations

The calculation of ion ranges and damage distributions is referred to as range calculations. In this thesis, a program MDRANGE [14] was used for range calculations to obtain the recoil spectrum of chromium ions irradiating tungsten, and the nuclear deposited energies. These were used for the atomic mixing calculations.

The MDRANGE algorithm is capable of calculating ion ranges from 100 eV to 100 keV and deposited energies [14]. In these ion range calculations, only the movement of the recoiling ion is followed. Hence, MDRANGE cannot be used to predict the details of the damage produced during implantation.

In order to make the simulation as efficient as possible, the algorithm

only accounts for the interactions between the ion and target atoms [14]. The interaction is taken into account only in the case when the distance to the target atom is above a certain cut-off, which is 2-3 Å in MDRANGE [14].

The interactions between atoms are described by repulsive universal ZBL potential developed by Ziegler et al. [54], where Coloumbic repulsion is modified by multiplying it with a screening function $\phi(r)$. At very small distances, the interaction could be described by pure Coloumbic repulsion without any multiplication since the electron clouds do not screen the nuclei from each other anymore [28]. The potential function is implemented as:

$$V_{ij}(r) = \frac{1}{4\pi\varepsilon}\frac{Z_1 Z_2 e^2}{r}\phi(r) \tag{3.14}$$

where Z_1 and Z_2 are the charges of the interacting atoms, r is the distance between the them, and $\phi(r)$ is the screening of the nuclei due to the electron cloud [28]. The screening function is given by:

$$\phi(r) = 0.1818e^{-3.2x} + 0.5099e^{-0.9423x} + 0.2802e^{-0.4029x} + 0.02817e^{-0.2016x} \tag{3.15}$$

where $x = r/a_u$, $a_u = (0.8854a_0)/(Z_1^0.23 + Z_2^0.23)$, and a_0 is the Bohr atomic radius, which is 0.529 Å [28].

The size of the simulation box also affects the efficiency of the calculations. The simulation box has to be large enough to hold all the atoms within the cut-off distance to the projectile. A system with a 10-15 Å cell side length and 50-100 atoms in the cell are usually sufficient to contain all the atoms that interact with the projectile [14]. As the projectile moves, the system is shifted, with pristine crystal generated in front of the projectile [14]. This way, fewer atoms and a smaller box can be used, and the simulation becomes more efficient.

Range calculations start by placing an initial recoil atom outside the simulation box by a few Å, and energy and velocity direction are given to it. The initial position of the recoil atom is chosen randomly, and its movement is followed through the whole simulation until a certain threshold energy is reached, for example, 1 eV. The movement of the recoiling atom is stored at each time step. Electronic stopping power is accounted for by reducing the projectile's velocity at each time step by an amount Δv, given by:

$$\Delta v = \Delta t \frac{S_e}{m} \tag{3.16}$$

Finally, after the simulations, the number of primary recoils per incident ion can be obtained as a function of recoil energy. Additionally, the nuclear energy loss is obtained by subtracting the electronic energy losses calculated by equation 3.16 from the total energy loss per distance travelled of the ion. The final deposited energy distribution can be obtained by averaging over each individual projectile trajectory. One needs to calculate the ion ranges for enough ions to obtain reliable results. In this thesis, the range calculations were calculated for 500 000 projectiles per initial condition.

4. Dissipation model

The dissipation model used in this thesis is implemented as a user package in LAMMPS. The aim of this work is to test the model's suitability for cascade simulations. The model is capable of describing the energy losses in all of the cascade processes from the ballistic phase to the thermal phase, accounting for the local environment dependent coupling to electrons [55]. However, the dissipation model extension in LAMMPS has a fifty percent higher computational cost compared to the conventional two-temperature model implemented in LAMMPS, since in this model, the non-trivial extra dissipative force needs to be calculated from the ion positions and velocities [55].

4.1 Two-temperature models in molecular dynamics simulations

In high-radiation events, through interactions of electrons with phonons and inelastic electronic scattering, the energy is transferred from the atomic system to the electronic system [56]. A part of the energy deposited in the electrons is returned to the atomic system, whereas another part is diffused through electrons, depending on the local temperature difference [56]. The non-equilibrium state between electrons and ions is expressed via heat diffusion equation. This method is called two-temperature model (TTM). The thermal diffusion equation can be numerically integrated in order to determine how the electronic energy changes over time and space [57]. In TTM's, at every time step of the MD simulations, the energy is exchanged between the atomic and the electronic systems.

In TTM models as also in the dissipation model used in this thesis, the

electronic subsystem is interpreted as a thermodynamic bath by the concept of the locality [55]. During the heat spike, the electrons could act either as a heat bath, adding energy to atoms, or conversely as a heat sink, scaling down energy from the atoms. However, usually for metals, the role is likely to be a heat sink [58], since when cold electrons move over the hot thermal spike area, energy is removed from the spike, which results in cooling of the spike. [49]. It can be thought of as a spatially modulated heat reservoir. In the simulations, the energy exchange between ionic and electronic systems is regulated via a source term Q_{e-i} as:

$$C_e \frac{\partial T_e}{t} = \nabla \cdot (\kappa_e \nabla T_e) + Q_{e-i} \tag{4.1}$$

$$Q_{e-i}(r) = \sum_I f_I^{e-i} * \boldsymbol{v_I} \gamma(\boldsymbol{r} - \boldsymbol{r_I}) \tag{4.2}$$

where C_e is the specific heat of electrons, T_e is the electron temperature, κ_e is the thermal conductivity of electrons, and Q_{e-i} is the source term, which couples the continuum electronic system to the ionic system.

4.2 Theory of the dissipation model

The issue with only considering electronic stopping power to account for electronic losses in the irradiation process is that during the heat spike, the dynamics of the atomic system change more into phonon-like behaviour [19]. In order to capture all the energy losses occurring between the ballistic and the thermal phase, the dissipation model accounts for the effects of the electron-phonon interactions as well as the electronic stopping power.

The model is a generalization of Langevin dynamics [59][60] which can be used to model electron-ion coupling for metals. The general format of the Langevin equation can be expressed as a function of three terms:

$$m\frac{\partial v_i}{\partial t} = F_i(t) - \gamma_i v_i + \mu(t) \tag{4.3}$$

where v_i is the velocity of ion i, F_i is the force acting on ion i at time t, $\gamma_i v_i$ is the friction term describing electronic stopping, and μ is the stochastic force at time t, which is obtained from the strength of the electron-phonon coupling [57]. However, in the general format of the Langevin equation, the electron-phonon coupling is given as a scalar value, which is not the case for the dissipation model used in this work.

In most cases, the electron-phonon coupling term in TTM-MD models is kept constant throughout the whole simulation [44]. However, when other studies have tried to determine the constant value for the strength of electron-phonon coupling, the estimates for any material vary significantly. There is over an order of magnitude difference between the estimates [61]. Hence, it is unclear which constant value should be chosen as a parameter as electron-phonon coupling strength in TTM-MD simulations. For better quantum mechanical results, the strength of electron-phonon coupling should be given as a function of the local electronic density [61].

For the dissipation model, both the friction term γ and stochastic force are represented with many-body forces acting in a correlated way on all particles in the system [47]. In this model, the force acting on atom i consists of three parts: the empirical potential's gradient, a viscous-like force, and a random force. The second and third terms are presented in a tensor format to incorporate correlations over the particles [55]. The force acting on each atom can be expressed as:

$$F_i = -\nabla_I U - \underbrace{\sum_J B_{IJ} v_j}_{\sigma_I} + \underbrace{\sum_J W_{IJ} \xi_J}_{\eta_I} \tag{4.4}$$

$$B_{IJ} = \sum_K W_{IK} W_{JK}^T \tag{4.5}$$

where the first term is an adiabatic force, which is independent of the electronic system, the second term σ_I and the third η_I are non-adiabatic forces derived from the ion-electron interactions. The second term σ_I is linear with velocities, and the third term η_I is stochastic [55]. Additionally, the source term Q_{e-i} is equivalent to the second term σ_I and the third term η_I [55].

The matrices W and B are functions of the particles' positions and represent the spatial correlation among the particles. ξ_J is white noise which is created by a thermal bath with local temperature T_e [55]. The random force η, which acts on a particle i in a particular direction, is statistically dependent on the other random forces [47]. Furthermore, the friction force σ is not an individual property of a particular particle, but it is a global property. In addition to statistical dependency, the friction force depends on other the particles' velocities as well [47].

The forces on individual ions are correlated spatially by combining white noise with a matrix W [55]. The matrix W_{IJ} is defined as:

$$W_{IJ} = \begin{cases} -\alpha_J(\rho_J)\frac{\rho_I(r_{IJ})}{\rho_J} e_{IJ}(\xi_J e_{IJ}) & I \neq J \\ \alpha_I(\rho_I)\sum_{k\neq I}\frac{\rho_K(r_{IK})}{\rho_I} e_{IK}(\xi_I e_{IK}) & I = J \end{cases} \tag{4.6}$$

where e_{IJ} is the unit vector that is linking the atoms with different indices, and $\alpha(\rho)$ is the coupling function describes the coupling strength of specific ions with the electron system [55]. The coupling parameter $\alpha(\rho)$ is purely a result of fitting data obtained by time-dependent density functional theory (TDDFT) calculations.

The dissipation model predicts relatively accurately the energy transferred collision by collision along the trajectory, but not point by point. This is due to the fact that in the model, frozen, spherical atomic densities are used instead of time-dependent ones [62]. However, if one used time-dependent atomic densities, there would be a significant increase in computation time. Therefore, this limitation is a cost of having a model that can be easily

implemented to MD simulations without increasing the computational cost too much.

5. Simulation methodology

5.1 Simulated values for ion-beam mixing

In this thesis, the simulations were done in parallel to increase the speed of the simulations. In parallel simulations, the domain is spatially distributed across processors, which communicate with each other by calling the message passing interface (MPI) [63]. LAMMPS can run very large simulations, up to billions of atoms and hundreds of processors, while simulating in parallel [64]. In the simulations of this thesis, there were up to nine million atoms and 48 processors utilized.

The simulated values for ion-beam mixing were obtained by two steps:

1. atomistic range calculations, and

2. full molecular dynamics simulations.

Range calculations were simulated in order to get the primary recoil spectrum of 1000 keV krypton (Kr) ions irradiating tungsten, and the deposited nuclear energy. Range calculations were done using the open-source range calculation program MDRANGE [14], developed at the Accelerator laboratory of the University of Helsinki by professor Kai Nordlund and his team. In the range simulations of this thesis, the recoil spectrum and deposited nuclear energy were calculated in the range of 200-600 Å. In the experiment of Kim et al. [65], the thickness of the layer was 5-15 Å, but for

Collision cascade runs per energy	
Energy (keV)	Amount of cascades simulations
0.04	100
0.07	100
0.1	100
0.4	50
1	50
2	50
5	50
10	50
20	50
50	30
100	30
150	30
200	20

Table 5.1. The amount of collision cascade simulations per energy.

range simulations, a broader range is necessary for accurate results since, the marker layer is broadened during Kr irradiation.

Full molecular dynamics simulations in 6 Kelvin were run to simulate collision cascades with different PKA energies. Simulations were done for energies in the range of 40 eV to 200 keV. A larger amount of collision cascades were simulated for lower energies than for higher energies, since the higher energy simulations were computationally more costly. The amounts of cascade simulations per energy are given in table 5.1.

From each energy, in each cascade simulation, square roots of displacements R^2 were obtained and averaged for every energy over all runs. The displacements were obtained from the difference between the initial positions of atoms after equilibrating the cell and the final position of atoms after the 75 picosecond cascade simulation. The displacements were calculated for every atom in the system and then multiplied together and squared to get the total squared atom displacements for every energy. The values were used as data points to fit the function in equation 2.5 which is needed for mixing efficiency calculation.

Finally, the mixing efficiency was calculated by constructing the results from these two-part simulations together. The cumulative atomic mixing efficiency resulting from Kr ions irradiating tungsten was calculated with

equation 2.6.

5.2 Different electron-phonon coupling strengths as a function of local electronic density in simulations

In this work, two different electron-phonon coupling strength functions were used in the MD simulations to see if they would result in different ion-beam mixing values. These two functions and their electron-phonon coupling strength in density can be seen in the figure 5.1.

The theoretical approximate constant value for the electron-phonon coupling strength g_{ep} is 0.01 $eV * ps/\text{Å}^2$ for both $\alpha(\rho)$ functions [47]. From figure 5.1 can be seen that the difference to the theoretical value for the electron-phonon coupling strength is quite significant, especially at very small electronic densities. The highest difference to the theoretical value is around 0.5 e/Å^3, where the function has its highest coupling strength approximately 0.07 $eV * ps/\text{Å}^2$. The electron-phonon coupling strength as a function of the local electronnic density should give better quantum mechanical results [55]. However, if the functions of the electron-phonon coupling strength were not accurately formed, the simulated values of atomic mixing would differ significantly from experimental ones.

The $\alpha(\rho)$ function 1 has a stronger coupling strength in lower $< 10^0$ electronic densities except when the local electronic density is around 10^{-1}. In larger electronic densities, the strength of the electron-phonon coupling is similar for both functions. The whole function goes to zero between 10^{-1} and 10^0. This is simply due to the result of the fitting procedure done by TDDFT calculations.

Electron-phonon coupling reduces atomic mixing [45]. When electrons and the lattice are coupled, heat from the hot cascade core is distributed to cooler electronic gas, suppressing the cascade core's liquid region. In that liquid region, atoms can redistribute and mix, and hence while it is suppressed, also atomic mixing reduces [45]. This indicates that a function with stronger electron-phonon coupling should give weaker results of atomic mixing and another way around. Hence, as the main differences between the functions $\alpha(\rho)$ are in the low electronic densities, there would be significant differences between simulated mixing efficiencies if

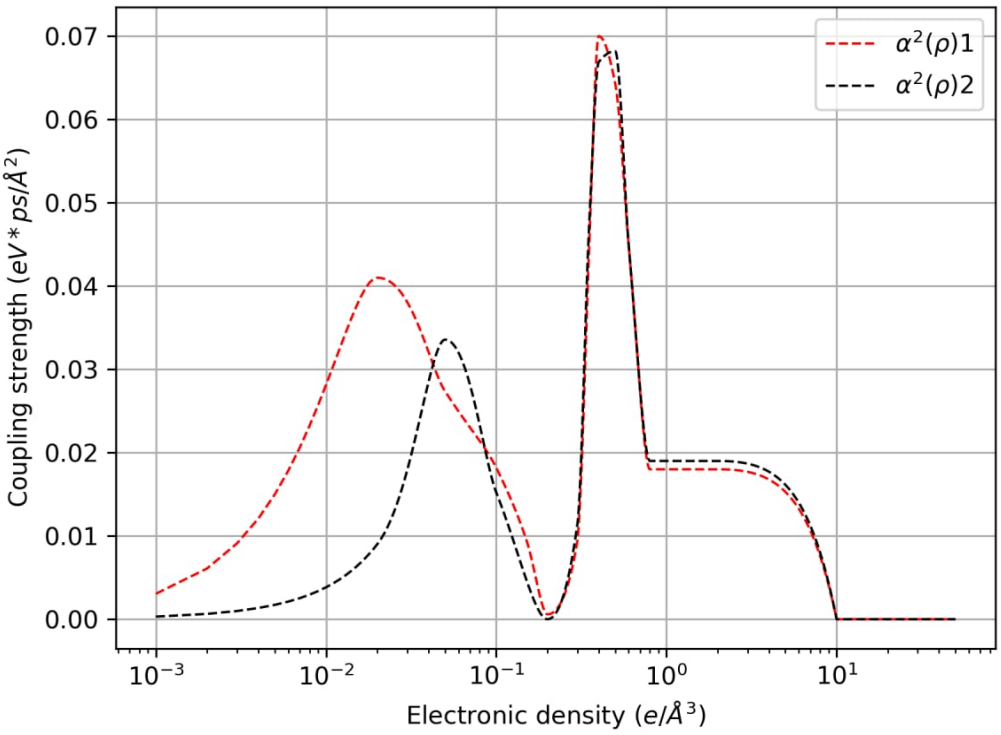

Figure 5.1. Different $\alpha(\rho)$ functions used in the full molecular dynamics simulations, and their electron-phonon coupling strength over electronic density.

the electron-phonon coupling strength was meaningful at low electronic densities.

6. Results

The purpose of this study was to test the viability of the dissipation model, which explicitly accounts for the electronic energy losses, in the highly non-equilibrium cascade process. This was done by performing atomistic simulations of radiation-induced collision cascades with methods specified in chapter 5. The level of ion-beam mixing is conjectured to be sensitive to the coupling between electronic and atomic systems. Hence, it was used to gauge the accuracy of the model. The atomistic mixing from simulations was analyzed and compared to Kim et al. [65] experimentally derived ion-beam mixing values for tungsten.

6.1 Simulated values for atomic mixing

The primary recoil spectrum for 1000 keV Kr ions bombarding tungsten is illustrated in figure 6.1. The deposited nuclear energy in depth of 200-600 Å of the Kr beam was 170891 eV.

The values of squared total displacements R^2 from both simulations using different electron-phonon coupling strength functions were quite close to each other at all energies. All values of R^2 are listed in the table 6.1. With the $\alpha(\rho)$ function 2, where the coupling strength was weaker at lower electronic densities, larger displacement values were obtained. Especially, from higher energy simulations, larger differences with the atomic displacements were obtained with the coupling function 2. At energies of 150 keV and on-wards, the differences between the atomic displacements differ with different functions for electron-phonon coupling.

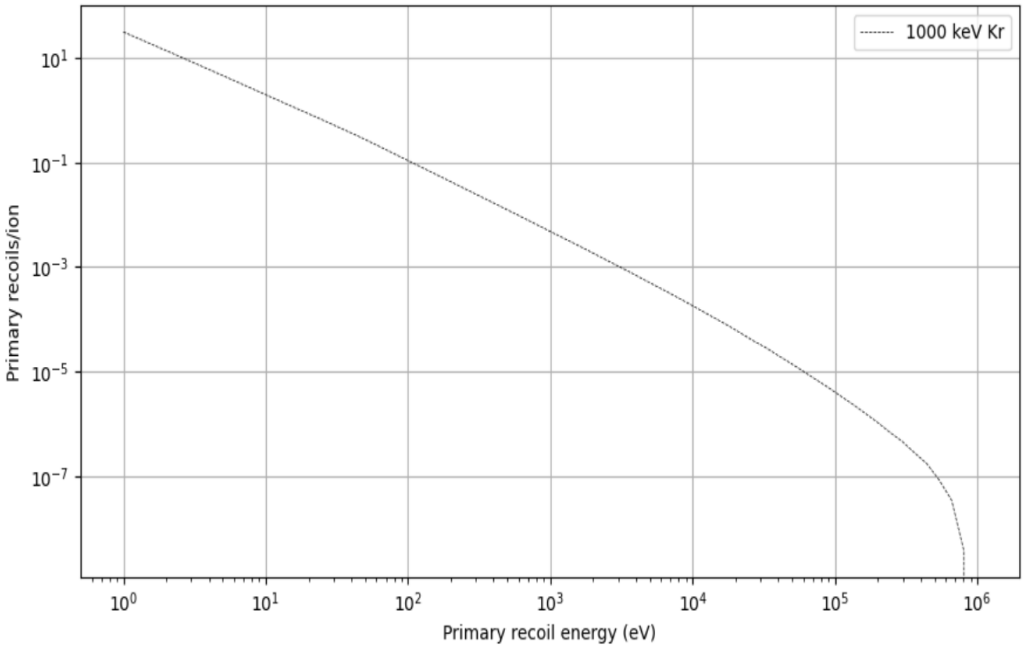

Figure 6.1. The primary recoil spectrum in depth of 200-600 Å. It is obtained by bombarding tungsten with 1000 keV Kr ions.

From figure 6.2 can be seen that both fitted functions are pretty similar until the very end 150 keV and 200 keV collision cascades. Additionally, the 70 eV and 100 eV collision cascades gave bigger displacements with coupling function 2.

Both simulated values of cumulative atomic mixing are shown in table 6.2. The results from simulations using the different functions for electron-phonon coupling are close to each other. Furthermore, the choice of the function does not give big differences in cumulative atomic mixing values.

The cumulative mixing efficiency as a function of primary recoil energy obtained with different electron-phonon coupling functions are illustrated in figure 6.3. From that figure, it can be seen that the mixing value is very close for both simulations until the higher energies. There is also a difference between the results when the energy is around $10^4 - 10^5$, but the difference is minimal. Moreover, the difference between the two cumulative mixing values comes from the displacements in the higher energy collision cascades.

R^2 values		
Energy (keV)	R^2 values obtained with $\alpha(\rho)$ function 1	R^2 values obtained with $\alpha(\rho)$ function 2
0.04	0±0	0±0
0.07	12.48±25.68	22.57±46.0
0.1	19.03±30.19	42.1±68.9
0.4	130.12±69.4	134.50±49.9
1.0	419.67±92.3	441.76±122.3
2.0	1024.04±196.6	1047.77±178.8
5.0	3879.47±581.1	3913.81±708.2
10.0	10551.24±1628.9	11821.98±2249.7
20.0	33189.38±19027.7	34489.98±12020.1
50	102133.77±37663.5	114824.45±25701.1
100	216250.05±65530.14	235071.88±40175.29
150	307136.05±40530.19	429597.48±83025.92
200	477237.17±70166.50	615202.86±194386.82

Table 6.1. Total average squared displacement values R^2 for every energy simulated and the standard deviations.

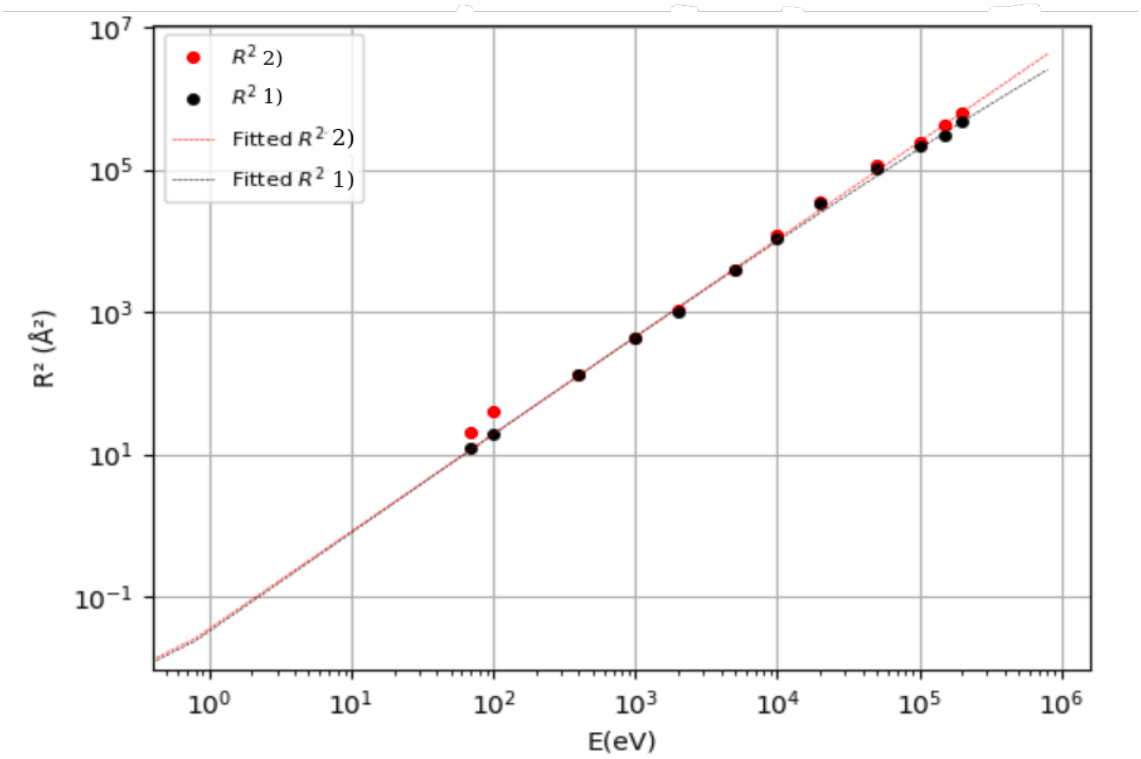

Figure 6.2. R^2 values with a fitted function from the simulation with different strength of electron-phonon coupling.

Q_{sim} values	
Q_{sim} values obtained with $\alpha(\rho)$ function 1	Q_{sim} values obtained with $\alpha(\rho)$ function 2
4.62	5.99

Table 6.2. Cumulative mixing efficiencies derived from the simulations for tungsten.

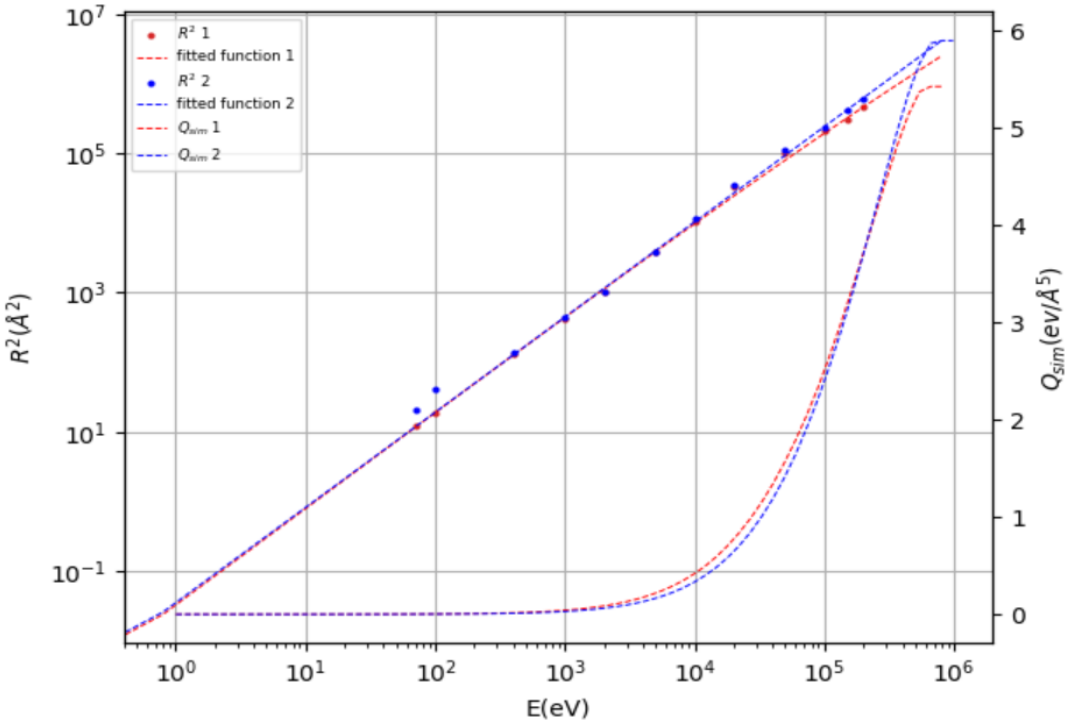

Figure 6.3. Q_{sim} and fitted functions from the simulation with different strength of electron-phonon coupling. The Q_{sim} 2 illustrate the atomic mixing efficiency when the function of electron-phonon coupling is slightly weaker, conversely the Q_{sim} 1 illustrate the atomic mixing efficiency when the function electron-phonon coupling is stronger.

6.2 Comparison to experiments

In the experimental procedure of Kim et al., a marker layer of nickel, iron, and yttrium, which were approximately 5-15 Å thick, was located in the mid-planes of 800 Å thick tungsten specimens. The specimens were then irradiated with 1000 keV Kr ions to doses of $10^{15} - 10^{16}$ $ions/cm^3$ at a constant temperature of 6 Kelvin. As a result of Kr irradiation, the marker layer broadened. From that broadening, the author measured the standard deviation to calculate the ion-beam mixing. The mixing efficiency in the experiment was calculated as illustrated in equation 2.3.

In the experiments, in order to avoid oxygen contamination, a silicon layer

Q_{exp} values	
Marker layer	Q_{exp}
Ni	17.9
Fe	7.5
Y	2.2

Table 6.3. Experimental values of ion-beam mixing for different marker layers used in tungsten experiments [65].

of approximately 30 Å was deposited on top of most specimens. Those samples, which did not have a silicon layer, might have experienced reactions with air when removed from the vacuum system. Kim et al. reported that in the experiments, the errors are mostly derived from the contamination of the specimens, not from inaccurate measurements. The measurement errors were estimated to be less than 15 percent in their experiments.

The experimental ion-beam mixing values of Kim et al. [65] are shown in table 6.3. These values vary for different marker layers. In figure 6.4, the experimental values and simulated values of atomic mixing are illustrated. The experimental atomic mixing values are represented with the ± 15 percent error bars. From that figure can be seen that both simulated values of atomic mixing settle almost at the middle of the three experimental values of atomic mixing.

The simulated values of atomic mixing differ from the experimental values where yttrium and nickel were used as a marker layer. Additionally, the experimental values with different marker layers differ from each other. This could be due to the heat of mixing. Negative values of heat of mixing give a positive driving force to the atomic mixing, which could lead to an increased atomic mixing value. The heats of mixing for all tungsten specimens from Kim et al. experimental studies are listed in table 6.4. For the specimen where iron was used as a marker layer, the heat of mixing value is zero. Both simulated mixing values are very close to that value, indicating for the correctness of simulated mixing values.

For the specimen where yttrium was used as a marker layer, the value for the heat of mixing (δ) was +110. This indicates for a strong driving force

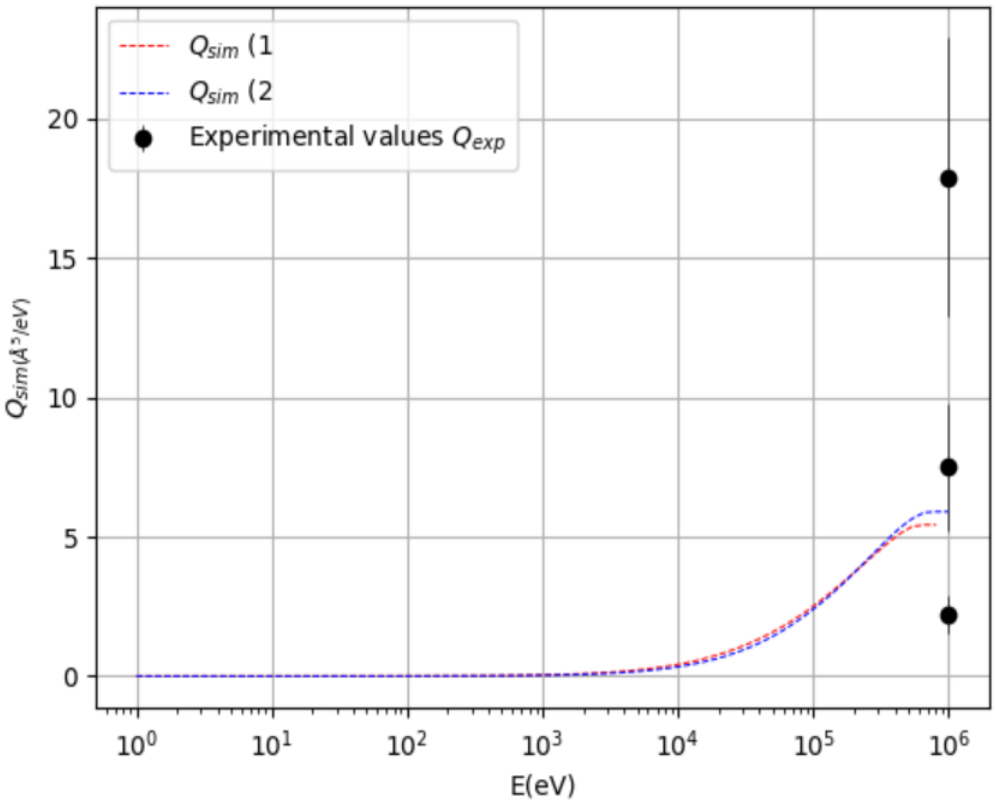

Figure 6.4. Simulated atomic mixing values Q_{sim} with different coupling functions $\alpha(\rho)$ and Kim et al. [65] experimentally obtained values Q_{exp} with $\pm$15 percent error bars.

for the atoms desiring to stay at their positions. Such high value of the heat of mixing could have decreased the atomic mixing in the experiments, explaining the low result for this specimen. Conversely, for the specimen where nickel was used as a marker layer, the heat of mixing was -11. In this case, there is a driving force for atoms to leave their positions, possibly increasing the atomic mixing. However, δ=-11 is not a very large value of heat of mixing. Hence, the heat of mixing is more likely to have an impact on the mixing efficiency of the specimen where yttrium was used as a marker layer.

Heat of mixing δ for different marker layers	
Marker layer	$\delta\ (kJ/mol)$
Ni	-11
Fe	0
Y	+110

Table 6.4. Heat of mixing for marker layers Ni, Fe, and Y, which were used in ion-beam mixing experiments [65].

7. Conclusions

In this thesis, molecular dynamics simulations were used to derive mixing efficiencies for tungsten, incorporating a newly developed two-temperature model which explicitly takes into account electronic losses due to both electronic stopping and electron-phonon interaction. Furthermore, since it is known that ion-beam mixing is sensitive to electron-phonon coupling, the mixing was calculated from atomistic simulations to gauge the accuracy of the model.

The simulated mixing efficiencies settle in the middle of the three experimental values of ion-beam mixing. The experimental value where the heat of mixing was zero was very close to the values of the simulated atomic mixing.

Additionally, the different functions of electron-phonon coupling strength did not have a significant effect on the atomic mixing. However, the other coupling function $\alpha(\rho)$ gave a slightly larger value for the mixing efficiency, which agreed with the experimental values even better.

Further work with the dissipation model, which accounts for electronic losses for metals, is essential. Now that it is gauged that the dissipation model works, the model's predictions should be investigated. Radiation damage from these simulations will be studied. Defects and defect clusters formed will be examined and compared to other methods.

8. Acknowledgments

Computational resources were provided by Aalto University Science-IT project. Atomistic simulations were done in Aalto high-performance computing cluster Triton.

Bibliography

[1] Z. Zhongming, L. Linong, Z. Wangqiang, L. Wei *et al.*, "Eia projects nearly 50% increase in world energy use by 2050, led by growth in renewables," 2021.

[2] S. J. Zinkle, "Fusion materials science: Overview of challenges and recent progress," *Physics of Plasmas*, vol. 12, no. 5, p. 058101, 2005.

[3] B. Wirth, K. Nordlund, D. Whyte, and D. Xu, "Fusion materials modeling: Challenges and opportunities," *MRS bulletin*, vol. 36, no. 3, pp. 216–222, 2011.

[4] K. Nordlund, S. J. Zinkle, A. E. Sand, F. Granberg, R. S. Averback, R. E. Stoller, T. Suzudo, L. Malerba, F. Banhart, W. J. Weber *et al.*, "Primary radiation damage: A review of current understanding and models," *Journal of Nuclear Materials*, vol. 512, pp. 450–479, 2018.

[5] G. Was, "Fundamentals of materials science: Metals and alloys," *Nuclear Engineering and Radiological Sciences, University of Michigan: Springer Berlin Heidelberg New York*, 2007.

[6] A. Sand, "Molecular dynamics simulations of primary radiation damage from collision cascades," Helsinki University, Doctoral dissertation, http://urn.fi/URN:ISBN:978-951-51-0586-8, 2015.

[7] R. Pitts, S. Carpentier, F. Escourbiac, T. Hirai, V. Komarov, S. Lisgo, A. Kukushkin, A. Loarte, M. Merola, A. S. Naik *et al.*, "A full tungsten divertor for iter: Physics issues and design status," *Journal of Nuclear Materials*, vol. 438, pp. S48–S56, 2013.

[8] S. Watanabe, S. Nogami, J. Reiser, M. Rieth, S. Sickinger, S. Baumgärtner, T. Miyazawa, and A. Hasegawa, "Tensile and impact properties of tungsten-rhenium alloy for plasma-facing components in fusion reactor," *Fusion Engineering and Design*, vol. 148, p. 111323, 2019.

[9] G. S. Was, "The radiation damage event," in *Fundamentals of Radiation Materials Science*. Springer, 2017, pp. 3–76.

[10] M. Norgett, M. Robinson, and I. M. Torrens, "A proposed method of calculating displacement dose rates," *Nuclear engineering and design*, vol. 33, no. 1, pp. 50–54, 1975.

[11] K. Nordlund, J. Wallenius, and L. Malerba, "Molecular dynamics simulations of threshold displacement energies in fe," *Nuclear Instruments and Methods*

in Physics Research Section B: Beam Interactions with Materials and Atoms, vol. 246, no. 2, pp. 322–332, 2006.

[12] N. Trung, H. Phuong, M. Starostenkov, V. Romanenko, and V. Popov, "Threshold displacement energy in ni, al and b2 nial," in *IOP Conference Series: Materials Science and Engineering*, vol. 447, no. 1. IOP Publishing, 2018, p. 012004.

[13] K. Nordlund, A. Sand, F. Granberg, S. Zinkle, R. Stoller, R. Averback, T. Suzudo, L. Malerba, F. Banhart, W. Weber *et al.*, "Primary radiation damage in materials," Report NEA/NSC/DOC, Tech. Rep., 2015.

[14] K. Nordlund, "Molecular dynamics simulation of ion ranges in the 1–100 kev energy range," *Computational materials science*, vol. 3, no. 4, pp. 448–456, 1995.

[15] A. Calder, D. J. Bacon, A. V. Barashev, and Y. N. Osetsky, "On the origin of large interstitial clusters in displacement cascades," *Philosophical Magazine*, vol. 90, no. 7-8, pp. 863–884, 2010.

[16] A. Sand, S. Dudarev, and K. Nordlund, "High- energy collision cascades in tungsten: Dislocation loops structure and clustering scaling laws," *EPL (Europhysics Letters)*, vol. 103, 06 2013.

[17] A. E. Sand, K. Nordlund, and S. Dudarev, "Radiation damage production in massive cascades initiated by fusion neutrons in tungsten," *Journal of Nuclear Materials*, vol. 455, no. 1-3, pp. 207–211, 2014.

[18] T. D. De La Rubia, R. S. Averback, R. Benedek, and W. King, "Role of thermal spikes in energetic displacement cascades," *Physical review letters*, vol. 59, no. 17, p. 1930, 1987.

[19] A. E. Sand, "Incorporating electronic effects in molecular dynamics simulations of neutron and ion-induced collision cascades," *Handbook of Materials Modeling: Applications: Current and Emerging Materials*, pp. 2413–2436, 2020.

[20] M. Nastasi, J. Mayer, and J. K. Hirvonen, *Ion beam mixing*, ser. Cambridge Solid State Science Series. Cambridge University Press, 1996, p. 295–331.

[21] K. Nordlund, M. Ghaly, and R. Averback, "Mechanisms of ion beam mixing in metals and semiconductors," *Journal of applied physics*, vol. 83, no. 3, pp. 1238–1246, 1998.

[22] B. Paine and R. S. Averback, "Ion beam mixing: basic experiments," *Nuclear Instruments and Methods in Physics Research Section B: Beam Interactions with Materials and Atoms*, vol. 7, pp. 666–675, 1985.

[23] S. Matteson and M. Nicolet, "Ion mixing," *Annual Review of Materials Science*, vol. 13, no. 1, pp. 339–362, 1983.

[24] A. E. Sand and K. Nordlund, "On the lower energy limit of electronic stopping in simulated collision cascades in ni, pd and pt," *Journal of Nuclear Materials*, vol. 456, pp. 99–105, 2015.

[25] N. Ashcroft and N. Mermin, "Solid state physics (saunders college)," *New York*, 1976.

[26] R. J. Tilley, *Defects in solids*. John Wiley & Sons, 2008, vol. 4.

[27] K, Nordlund, "Defect types — from wikimedia commons, the free media repository," 2007, [Online; accessed 2-Decemberr-2021]. [Online]. Available: https://commons.wikimedia.org/wiki/File:Defecttypes.png

[28] K. Nordlund, "Energy loss of energetic ions," *The Accelerator Laboratory at University of Helsinki*, vol. 30, 1996.

[29] M. Backman *et al.*, "Effects of nuclear and electronic stopping power on ion irradiation of silicon-based compounds," 2012.

[30] I. Lifshits, M. Kaganov, and L. Tanatarov, "On the theory of radiation-induced changes in metals," *Journal of Nuclear Energy. Part A. Reactor Science*, vol. 12, no. 1-2, pp. 69–78, 1960.

[31] K, Nordlund, "Molecular dynamics algorithm — from wikimedia commons, the free media repository," 2015, [Online; accessed 1-October-2021]. [Online]. Available: https://commons.wikimedia.org/w/index.php?curid=41419953s

[32] D. C. Rapaport, *The art of molecular dynamics simulation*. Cambridge university press, 2004.

[33] A. P. Thompson, H. M. Aktulga, R. Berger, D. S. Bolintineanu, W. M. Brown, P. S. Crozier, P. J. in 't Veld, A. Kohlmeyer, S. G. Moore, T. D. Nguyen, R. Shan, M. J. Stevens, J. Tranchida, C. Trott, and S. J. Plimpton, "LAMMPS - a flexible simulation tool for particle-based materials modeling at the atomic, meso, and continuum scales," *Comp. Phys. Comm.*, vol. 271, p. 108171, 2022.

[34] J. C. Jo and B. C. Kim, "Determination of proper time step for molecular dynamics simulation," *Bulletin of the Korean Chemical Society*, vol. 21, no. 4, pp. 419–424, 2000.

[35] K. Choudhary, F. Y. P. Congo, T. Liang, C. Becker, R. G. Hennig, and F. Tavazza, "Evaluation and comparison of classical interatomic potentials through a user-friendly interactive web-interface," *Scientific data*, vol. 4, no. 1, pp. 1–12, 2017.

[36] K. Nordlund and S. L. Dudarev, "Interatomic potentials for simulating radiation damage effects in metals," *Comptes Rendus Physique*, vol. 9, no. 3-4, pp. 343–352, 2008.

[37] J. Byggmästar, M. Nagel, K. Albe, K. O. E. Henriksson, and K. Nordlund, "Analytical interatomic bond-order potential for simulations of oxygen defects in iron," *Journal of Physics: Condensed Matter*, vol. 31, no. 21, p. 215401, 2019.

[38] J. M. Haile, I. Johnston, A. J. Mallinckrodt, and S. McKay, "Molecular dynamics simulation: elementary methods," *Computers in Physics*, vol. 7, no. 6, pp. 625–625, 1993.

[39] J. Byggmästar, "Development of interatomic potentials in the tersoff-albe formalism for metal compounds," Helsinki University MSc Thesis http://hdl.handle.net/10138/166468, 2016.

[40] M. Finnis and J. Sinclair, "A simple empirical n-body potential for transition metals," *Philosophical Magazine A*, vol. 50, no. 1, pp. 45–55, 1984.

[41] G. Ackland and R. Thetford, "An improved n-body semi-empirical model for body-centred cubic transition metals," *Philosophical Magazine A*, vol. 56, no. 1, pp. 15–30, 1987.

[42] G. Ackland, A. Sutton, and V. Vitek, "Twenty five years of finnis–sinclair potentials," 2009.

[43] M. I. Baskes, "Modified embedded-atom potentials for cubic materials and impurities," *Physical review B*, vol. 46, no. 5, p. 2727, 1992.

[44] A. Tamm, G. Samolyuk, A. Correa, M. Klintenberg, A. Aabloo, and A. Caro, "Electron-phonon interaction within classical molecular dynamics," *Physical Review B*, vol. 94, no. 2, p. 024305, 2016.

[45] C. Björkas and K. Nordlund, "Assessment of the relation between ion beam mixing, electron–phonon coupling and damage production in fe," *Nuclear Instruments and Methods in Physics Research Section B: Beam Interactions with Materials and Atoms*, vol. 267, no. 10, pp. 1830–1836, 2009.

[46] E. Zarkadoula, D. M. Duffy, K. Nordlund, M. A. Seaton, I. T. Todorov, W. J. Weber, and K. Trachenko, "Electronic effects in high-energy radiation damage in tungsten," *Journal of Physics: Condensed Matter*, vol. 27, no. 13, p. 135401, 2015.

[47] A. Tamm, M. Caro, A. Caro, G. Samolyuk, M. Klintenberg, and A. A. Correa, "Langevin dynamics with spatial correlations as a model for electron-phonon coupling," *Physical review letters*, vol. 120, no. 18, p. 185501, 2018.

[48] K. Nordlund, L. Wei, Y. Zhong, and R. Averback, "Role of electron-phonon coupling on collision cascade development in ni, pd, and pt," *Physical Review B*, vol. 57, no. 22, p. R13965, 1998.

[49] C. Flynn and R. S. Averback, "Electron-phonon interactions in energetic displacement cascades," *Physical Review B*, vol. 38, no. 10, p. 7118, 1988.

[50] M. Finnis, P. Agnew, and A. Foreman, "Thermal excitation of electrons in energetic displacement cascades," *Physical Review B*, vol. 44, no. 2, p. 567, 1991.

[51] F. Gao, D. Bacon, P. Flewitt, and T. Lewis, "The effects of electron-phonon coupling on defect production by displacement cascades in-iron," *Modelling and Simulation in Materials Science and Engineering*, vol. 6, no. 5, p. 543, 1998.

[52] V. Rühle, "Berendsen and nose-hoover thermostats," *Am. J. Phys*, 2007.

[53] H. J. Berendsen, J. v. Postma, W. F. van Gunsteren, A. DiNola, and J. R. Haak, "Molecular dynamics with coupling to an external bath," *The Journal of chemical physics*, vol. 81, no. 8, pp. 3684–3690, 1984.

[54] J. F. Ziegler and J. P. Biersack, "The stopping and range of ions in matter," in *Treatise on heavy-ion science*. Springer, 1985, pp. 93–129.

[55] A. Tamm, M. Caro, A. Caro, and A. Correa, "Role of electrons in collision cascades in solids. ii. molecular dynamics," *Physical Review B*, vol. 99, no. 17, p. 174302, 2019.

[56] E. Zarkadoula, G. Samolyuk, and W. J. Weber, "Two-temperature model in molecular dynamics simulations of cascades in ni-based alloys," *Journal of Alloys and Compounds*, vol. 700, pp. 106–112, 2017.

[57] D. Duffy and A. Rutherford, "Including the effects of electronic stopping and electron–ion interactions in radiation damage simulations," *Journal of Physics: Condensed Matter*, vol. 19, no. 1, p. 016207, 2006.

[58] A. Stoneham, "Energy transfer between electrons and ions in collision cascades in solids," *Nuclear Instruments and Methods in Physics Research Section B: Beam Interactions with Materials and Atoms*, vol. 48, no. 1-4, pp. 389–398, 1990.

[59] P. Langevin, "Sur la théorie du mouvement brownien," *Compt. Rendus*, vol. 146, pp. 530–533, 1908.

[60] D. S. Lemons and A. Gythiel, "Paul langevin's 1908 paper "on the theory of brownian motion"["sur la théorie du mouvement brownien," cr acad. sci.(paris) 146, 530–533 (1908)]," *American Journal of Physics*, vol. 65, no. 11, pp. 1079–1081, 1997.

[61] C. Race, D. Mason, M. Finnis, W. Foulkes, A. Horsfield, and A. Sutton, "The treatment of electronic excitations in atomistic models of radiation damage in metals," *Reports on Progress in Physics*, vol. 73, no. 11, p. 116501, 2010.

[62] M. Caro, A. Tamm, A. Correa, and A. Caro, "Role of electrons in collision cascades in solids. i. dissipative model," *Physical Review B*, vol. 99, no. 17, p. 174301, 2019.

[63] B. FrantzDale, S. J. Plimpton, and M. S. Shephard, "Software components for parallel multiscale simulation: an example with lammps," *Engineering with Computers*, vol. 26, no. 2, pp. 205–211, 2010.

[64] Plimpton SJ, "Lammps benchmarks," 2008, [Online; accessed 6-Decemberr-2021]. [Online]. Available: https://www.lammps.org/bench.html

[65] S.-J. Kim, M. Nicolet, R. Averback, and D. Peak, "Low-temperature ion-beam mixing in metals," *Physical Review B*, vol. 37, no. 1, p. 38, 1988.